Earth and Planetary Science Letters 474 (2017) 368–374

Contents lists available at ScienceDirect

Earth and Planetary Science Letters

www.elsevier.com/locate/epsl

Oriented grain growth and modification of 'frozen anisotropy' in the lithospheric mantle

Yuval Boneh [a,*], David Wallis [b], Lars N. Hansen [b], Mike J. Krawczynski [a], Philip Skemer [a]

[a] Washington University in St. Louis, Earth and Planetary Sciences, One-Brookings Drive, Campus Box 1169, Saint Louis, MO 63130, United States
[b] Oxford University, Department of Earth Sciences, Oxford, United Kingdom

ARTICLE INFO

Article history:
Received 14 April 2017
Received in revised form 25 June 2017
Accepted 29 June 2017
Available online 21 July 2017
Editor: J. Brodholt

Keywords:
olivine
crystallographic preferred orientation
grain growth
seismic anisotropy
mantle lithosphere

ABSTRACT

Seismic anisotropy throughout the oceanic lithosphere is often assumed to be generated by fossilized texture formed during deformation at asthenospheric temperatures close to the ridge. Here we investigate the effect of high-temperature and high-pressure static annealing on the texture of previously deformed olivine aggregates to simulate residence of deformed peridotite in the lithosphere. Our experiments indicate that the orientation and magnitude of crystallographic preferred orientation (CPO) will evolve due to the preferential growth of grains with low dislocation densities. These observations suggest that texture and stored elastic strain energy promote a style of grain growth that modifies the CPO of a deformed aggregate. We demonstrate that these microstructural changes alter the orientation distributions and magnitudes of seismic wave velocities and anisotropy. Therefore, static annealing may complicate the inference of past deformation kinematics from seismic anisotropy in the lithosphere.

© 2017 The Authors. Published by Elsevier B.V. This is an open access article under the CC BY license (http://creativecommons.org/licenses/by/4.0/).

1. Introduction

The upper mantle is seismically anisotropic (e.g., Burgos et al., 2014), which is mainly attributed to elastically anisotropic olivine crystals aligned in a crystallographic preferred orientation (CPO) (e.g., Nicolas and Christensen, 1987). CPO in olivine is typically interpreted to result from solid-state plastic deformation. As such, interpretation of seismic anisotropy is the primary approach for inferring the kinematics of mantle flow (Karato et al., 2008; Skemer and Hansen, 2016).

The interpretation of seismic anisotropy is particularly challenging near plate boundaries, where flow patterns are complex (Boneh and Skemer, 2014; Skemer et al., 2012). However, even beneath the interiors of oceanic plates, which are assumed to be kinematically simple, there is still vigorous debate about the depths, magnitudes, and orientations of seismic anisotropy (Becker et al., 2014; Lin et al., 2016). Many studies assume that the orientation of anisotropy in the highly viscous lithospheric mantle is "locked-in" and records the kinematics of deformation during its formation at the mid-ocean ridge, while anisotropy in the asthenosphere is continuously overprinted by current plate motion. This basic model is supported by numerous studies that detect layered anisotropy in both the oceanic and continental lithosphere (Barruol et al., 1997; Silver and Chan, 1991; Silver and Savage, 1994; Yuan and Romanowicz, 2010).

However, the validity of this model rests on two assumptions: first, that due to temperature-dependent changes in rock rheology the mantle does not deform significantly below a certain temperature, and second, that deformation is the only process that affects CPO. Here, we explore this second assumption by investigating the influence of high temperature and high pressure static annealing on the stability of olivine CPO.

2. Methods

The starting material for these experiments was a synthetic Fo_{50} olivine aggregate, which was previously deformed in torsion at a confining pressure of 0.3 GPa and 1200 °C in a Paterson apparatus at the University of Minnesota (sample PT0718; for full description of the sample fabrication and deformation see: Hansen et al., 2016). Fo_{50} is a reliable analogue to Fo_{90} olivine in terms of its mechanical and textural behavior, but has a lower viscosity under the same deformation conditions, which facilitates high shear strain torsion experiments (Hansen et al., 2014; Zhao et al., 2009). We cut the deformed sample into three equal-sized slices along longitudinal sections parallel to both the radial direction and the axis of the initially cylindrical sample. As the sample was deformed in torsion, there is a linear gradient in shear strain from the outer edge to the center of the cylinder. The por-

* Corresponding author.
E-mail addresses: boneh@levee.wustl.edu (Y. Boneh), david.wallis@earth.ox.ac.uk (D. Wallis), lars.hansen@earth.ox.ac.uk (L.N. Hansen), mikekraw@wustl.edu (M.J. Krawczynski), pskemer@wustl.edu (P. Skemer).

http://dx.doi.org/10.1016/j.epsl.2017.06.050
0012-821X/© 2017 The Authors. Published by Elsevier B.V. This is an open access article under the CC BY license (http://creativecommons.org/licenses/by/4.0/).

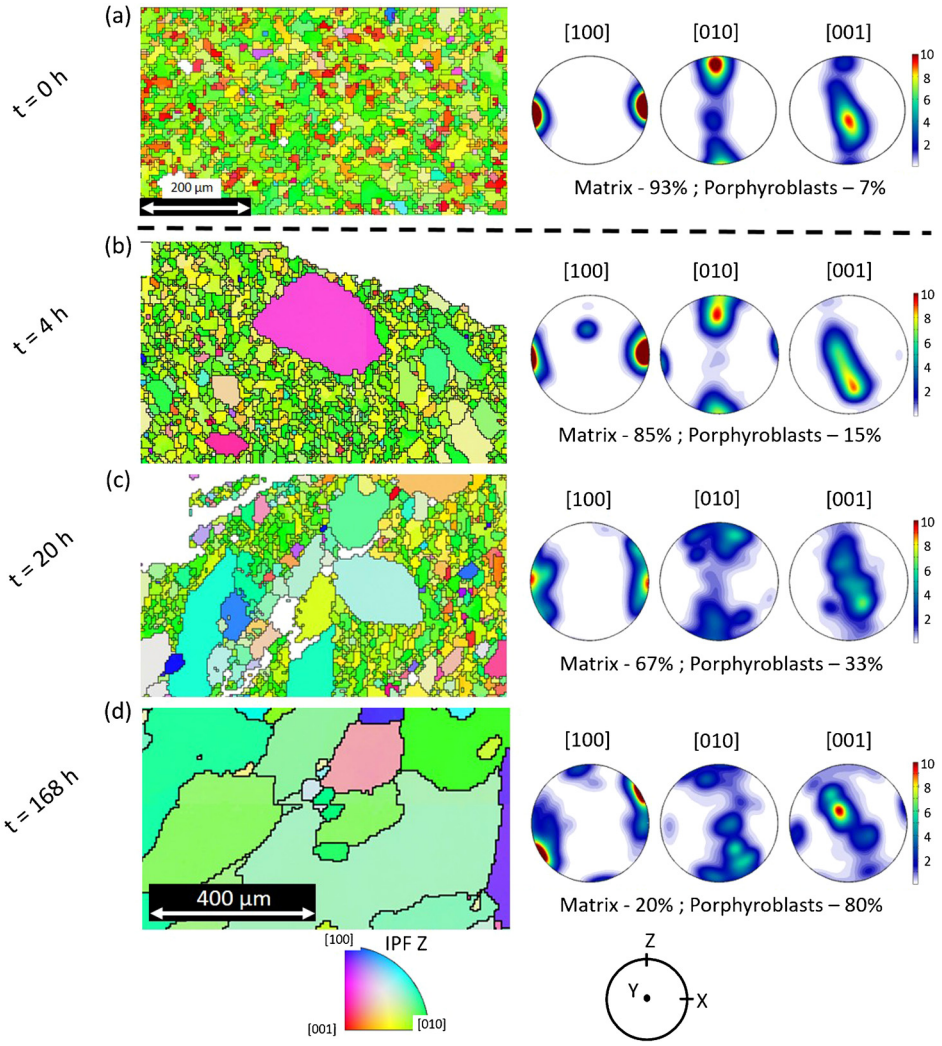

Fig. 1. Electron backscatter diffraction (EBSD) maps for (a) starting, initially deformed sample, and samples annealed for (b) 4 h, (c) 20 h, and (d) 168 h. Grain colors represent the orientation of the olivine crystal axes with respect to the normal to the shear plane (the Z-axis). Upper hemisphere pole figures show the associated crystallographic preferred orientation (CPO) of olivine where colors represent multiples of uniform distribution. Area fraction of matrix grains ($d < 100$ µm) and porphyroblasts ($d > 100$ µm) for each map is given in percentage beneath the corresponding pole figures.

tions of the sample used in this study were deformed to shear strains from $\gamma = 7$–10.

Following the torsional deformation, olivine grains in the sample are 11 ± 8 µm in diameter, with aspect ratios of approximately 2:1. The olivine CPO is strong, with [100] axes parallel to the shear direction and [010] axes perpendicular to the shear plane, which corresponds to the A-type CPO of Jung and Karato (2001) (Fig. 1a). The narrow size distribution of dynamically recrystallized grains, the strength of the CPO, and comparison to samples deformed to a wide range of strains in similar experiments suggest that the microstructure is near steady-state (Hansen et al., 2014).

In the annealing stage of the experiments, the samples were held at constant temperature and hydrostatic pressure, using $BaCO_3$ and MgO as the pressure medium and spacers respectively, in a solid-medium piston-cylinder apparatus. Each sample was surrounded with Fo_{50} powder, which was identical to the powder used to synthesize the original sample, and packed inside a nickel capsule. The three samples were annealed at 1 GPa and 1250 °C for 4, 20, or 168 h, respectively. During each run, pressure was increased to 1 GPa at room temperature and then temperature was increased by 50 °C per min with a 6-min pause at 900 °C to allow the system to stabilize. Samples were quenched by shutting off the power to the furnace, which reduces the sample temperature to less than 100 °C in under 30 seconds.

Thick sections of the annealed samples were prepared with a cross sectional area of ~1 mm^2 oriented parallel to the $Y-Z$ plane of the starting deformed sample, i.e., within the plane that includes the radial direction (Y-axis) and the normal to the shear plane (Z-axis), and perpendicular to the shear direction (X-axis) (Fig. 1). Samples were polished using SiC and diamond abrasives down to 0.25 micron, followed by chemical–mechanical polishing using colloidal silica. Microstructural elements including grain size, intra- and inter-granular misorientation, and crystallographic orientation were characterized in two stages. First, large areas were mapped using conventional electron backscatter diffraction (EBSD). These data were acquired using a JEOL 7001-FLV scanning electron microscope (SEM) at 20 kV with an Oxford Instruments Nordlys F+ EBSD detector. Second, key areas were selected and mapped using high-angular resolution EBSD (HR-EBSD, Wallis et al., 2016; Wilkinson et al., 2006). These data were acquired using an FEI Quanta 650 field emission gun SEM at 30 kV with an Oxford Instruments Nordlys S EBSD detector. All data were acquired with SEMs operated in low-vacuum mode. EBSD maps have a step size of either 1 or 5 microns and HR-EBSD maps have a step size of 0.6 µm. Data were analyzed using Oxford Instruments

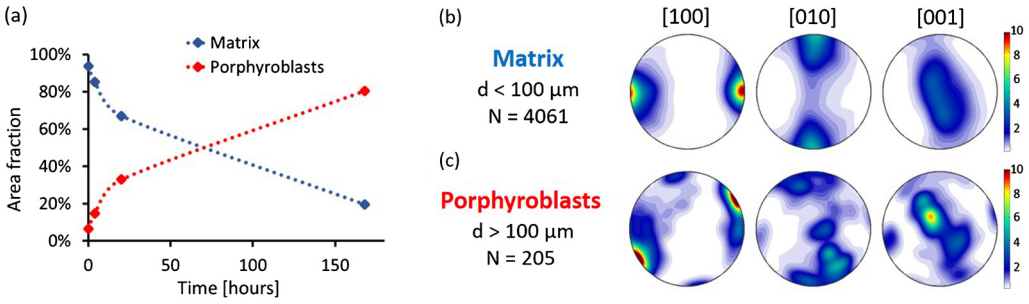

Fig. 2. (a) Evolution of area fraction comprised of matrix or porphyroblasts from the three annealing samples plotted against annealing time. (b) and (c) Pole figures showing the combined crystallographic preferred orientation (CPOs) of (b) matrix grains and (c) porphyroblasts, where colors represent multiples of uniform distribution. (For interpretation of the references to color in this figure, the reader is referred to the web version of this article.)

HKL software and MTEX – a MATLAB based toolbox for analyzing crystallographic textures (Mainprice et al., 2014). Extrapolation of unindexed pixels was performed using an HKL noise reduction algorithm, in which pixels with five adjacent pixels with common orientation were filled. Selected additional extrapolation was conducted manually, using band-contrast imaging to identify boundaries between grains. HR-EBSD post-processing uses cross-correlation of regions of interest in diffraction patterns to measure lattice curvature with angular resolution of ∼0.01° (Wilkinson et al., 2006). The lattice curvature is used to estimate densities of geometrically necessary dislocations (GNDs). See Wallis et al. (2016) for further details of this method.

3. Results

Experimental samples show a distinct and progressive change in microstructure as a function of the duration of static annealing. These microstructural changes include an evolution of the grain-size distribution and a marked change in dislocation density. Fig. 1 presents representative EBSD maps of the grain-scale microstructure and pole figures of the CPO of the starting, initially deformed sample, and of samples F052, F042, and F037, which were annealed for 4, 20, and 168 h, respectively. Sample F052, annealed for 4 h (Fig. 1b), contains large domains of grains that are comparable in size to the starting material (hereafter referred to as 'matrix'). Within this matrix are embedded a small number of grains, each about an order of magnitude larger than matrix grains (hereafter referred to as 'porphyroblasts'), which have grown rapidly at the expense of matrix grains. We distinguish the two groups using a threshold of 100 µm, with grains smaller than 100 µm defined as matrix, and grains larger than 100 µm defined as porphyroblasts. Sample F042, annealed for 20 h (Fig. 1c), exhibits a similar bimodal grain-size distribution, but with a larger areal fraction of porphyroblasts. Sample F037, which was annealed for 168 h (Fig. 1d), is almost entirely composed of large porphyroblasts (0.5–2 mm), with only a few remnant matrix grains. Fig. 2a displays the evolution of area fraction occupied by the matrix (blue line) and the porphyroblasts (red line).

Crystallographic data are presented as pole figures depicting the orientation of [100], [010] and [001] axes from each pixel in the original deformation reference frame (Fig. 1). The complete data set, in which each pixel is represented equally in the pole figures, is used to capture the relative importance of the larger grains when the grain-size distribution is bimodal. The starting CPO is a strong A-type with the [100] axis oriented parallel to the shear direction (X-axis), indicative of grain rotations dominated by slip on the (010)[100] system. After 4 h of annealing, there is some dispersion of the original CPO that corresponds to the addition of the orientations of the growing porphyroblasts (Fig. 1b). After 20 h of annealing, the original CPO is still clearly evident, but with the addition of a new secondary [100] peak at a small angle to the shear direction (Fig. 1c). After 168 h of annealing, the dominant peak in the [100] pole figure shifts to a new orientation that is ∼10–15° from the shear direction; only a weak peak remains parallel to the X-axis. The porphyroblasts comprise more than 80% of the sample area and therefore dominate the overall texture (Fig. 1d).

Data are combined from the three annealing experiments to show how CPO of the matrix population compares to the porphyroblast population (Fig. 2). The matrix exhibits a simple orthorhombic CPO pattern (Fig. 2b) similar to the starting material (Fig. 1a). The porphyroblast CPO is more complex (Fig. 2c). It is characterized by peaks that are rotated ∼10–15° from the matrix orientation, with some additional peaks oriented at a high angle (∼100–110°) to the matrix CPO. The different groups of crystallographic orientations can be seen most clearly in the [100] pole figure. The primary point maximum is oriented at a 10–15° angle from the shear direction (within the $X-Z$ plane). A secondary point maximum arises from a group of crystals with [100] axes oriented parallel to the shear direction, and are similar to the CPO of the matrix. There is also a set of crystals with [100] axes oriented ∼100–110° to the shear plane at a small angle to the Z-axis. The [010] pole figure contains grains oriented either in the original orientation, with [010] normal to the shear plane (parallel to Z), or rotated away from Z towards the Y-axis. The [001] pole figure exhibits a dominant point maximum parallel to the Y-axis with two additional prominent maxima 90° from each other on the $X-Z$ plane.

Fig. 3 displays a single porphyroblast from sample F052 (marked by a red star) surrounded by matrix on three sides. The porphyroblast is characterized by generally straight boundaries that are cuspate in a few locations where the boundary is enveloping small relict matrix grains. In contrast, the matrix grains have bulging grain-boundaries that are similar to those observed in the starting material (Fig. 3a, c). The porphyroblast orientation is rotated 90° about the Y-axis from the matrix orientation, with [100] oriented normal to the original slip plane and the [010] axis oriented towards the shear direction (Fig. 3b). The porphyroblast has a mean apparent GND density of 5.2×10^{12} m^{-2}. This density is at the noise level of the measurement for the mapping step size used (Wallis et al., 2016) and therefore represents an upper bound on the GND density within the porphyroblast. In contrast, the matrix has a mean GND density of 5.7×10^{14} m^{-2}, which is at least two orders of magnitude greater than the GND density of the porphyroblast and does not appear to be significantly modified by the annealing process. The boundaries between the porphyroblast and the matrix are typically high angle, with misorientation angles between 75 and 110°. In contrast, boundaries within the matrix, which still retains a strong CPO, have an average misorientation angle of 30° with standard deviation of 16° (Fig. 3c). A compilation of the grain-boundary misorientations from all three samples exhibits a clear shift in the overall distribution from grain bound-

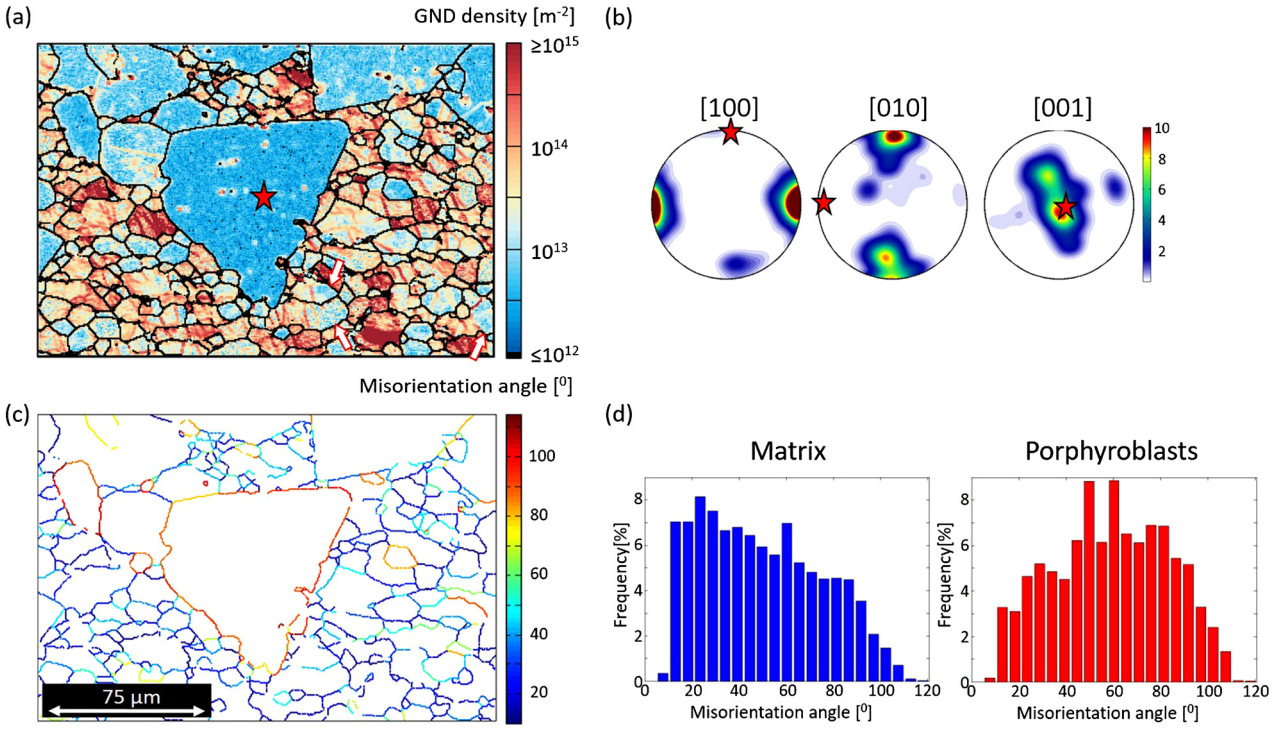

Fig. 3. (a) Densities of geometrically necessary dislocations (GNDs) estimated from high-angular resolution electron backscatter diffraction data. A notable porphyroblast is marked with a red star. Some elongate matrix grains with spatial variation in dislocation density, possibly representing the initial stage of primary grain boundary migration, are marked with white arrows. (b) Pole figures showing the CPO of the analyzed area excluding the porphyroblast, which is marked as a red star, where pole figures colors represent multiples of uniform distribution. (c) Map of the same area as (a) highlighting grain boundary misorientation angles. (d) Distribution of grain boundary misorientation angles between the matrix and porphyroblast grains. (For interpretation of the references to color in this figure legend, the reader is referred to the web version of this article.)

aries with low misorientation for matrix grains to grain boundaries with high misorientation for the porphyroblasts (Fig. 3d).

4. Discussion

4.1. Interpretation of microstructural observations

Static annealing of polycrystalline materials involves a variety of processes, including dislocation annihilation and grain growth, both of which decrease the total energy stored in the material. Studies of the kinetics of grain growth in synthetic olivine aggregates typically show evidence for grain growth in which the grain-size distribution remains narrow, with a log-normal distribution (Karato, 1989; Nichols and Mackwell, 1991). This type of grain growth is generally referred to as (spatially) continuous or 'normal', reflecting the continuous shift of unimodal grain-size distribution as the mean grain-size increases (e.g., Atkinson, 1988). However, in starting materials that are less homogeneous, grain growth may proceed by (spatially) discontinuous or 'abnormal' grain growth, reflecting the rapid growth of selected grains during a transient stage characterized by a highly bimodal grain-size distribution (e.g., Hillert, 1965). The noticeable microstructural evolution in our experiments, from an initially homogeneous microstructure with grain sizes around 30 µm and curved grain boundaries, to a microstructure that is dominated by grains that are 100–1000 µm in diameter with straight grain boundaries (Figs. 1–3), is typical of discontinuous grain-growth. Cooper and Kohlstedt (1984) have observed discontinuous grain growth in olivine aggregates comprised of 4 or 10% basaltic melt and some initial larger grains. Although the driving forces for grain-boundary migration (GBM) in Cooper and Kohlstedt are different compared with this study, the intrinsic calculated mobilities are similar (for the grain-boundary mobility calculations see Appendix A).

For grains to grow discontinuously at the expense of other grains, two conditions must be met: (1) before discontinuous growth commences, a small number of grains in the aggregate must be larger than other grains, by at least a factor of two (Hillert, 1965), and (2) the kinetics of growth of the matrix (relict small grains) must be intrinsically slow or inhibited. In our experiments, the low dislocation-density of the porphyroblasts suggests that a small, selective group of grains with relatively low dislocation-density grew rapidly at the expense of neighboring grains with high dislocation-density during the initial stages of annealing. This primary stage of growth, driven by gradients in strain energy associated with the dislocation content, produced a set of grains that are roughly double the size of their neighbors, satisfying the first condition for discontinuous grain-growth. Fig. 3a contains some examples of larger, elongate grains with gradients in dislocation density, which are interpreted to be examples of grains with boundaries that have migrated during the primary stage of recovery. For the second condition, a mechanism for inhibiting grain growth of matrix grains is needed. There are several mechanisms by which grain growth can be inhibited or slowed, including pinning of grain boundaries by secondary phases (Evans et al., 2001; Rios, 1997), the presence of impurities at grain boundaries (Bhattacharyya et al., 2015; Powers and Glaeser, 1998; Skemer and Karato, 2007), and the presence of a strong CPO yielding mostly low angle grain boundaries and low mean surface energy (Abbruzzese and Lücke, 1986; Eichelkraut et al., 1988). Since low surface energy is directly related to the driving force for grain boundary migration (eq. (2) in Appendix A) and sample PT0718 is nearly monomineralic and chemically homogeneous, it is unlikely that secondary phases or impurities play a significant role in the inhibition of GBM. In addition, randomly oriented grains used to synthesize the deformed sample were hot-pressed during the hydrostatic experiments, showed only weak coarsening with

no evidence for discontinuous grain growth (Supplementary material, Fig. S1). Therefore we infer that strong CPO is the explanation for the inhibition of normal grain-growth in our experiments, which is consistent with theoretical predictions (Abbruzzese and Lücke, 1986; Eichelkraut et al., 1988; Humphreys, 1997; Novikov and Novikov, 1997, pp. 102–111; Rollett et al., 1989) and experimental observations (Kim et al., 2007; Mishin et al., 2010; Zahid et al., 2009).

4.2. CPO modification during static annealing – comparison with previous studies

The results presented here indicate that static annealing of olivine results in discontinuous grain growth and both weakens and rotates pre-existing CPO. Previous studies spanning several geologic materials that investigated the style of static grain growth and the degree to which the strength and orientation of CPO is modified came to varied conclusions. Heilbronner and Tullis (2002) performed post-deformation annealing experiments on quartzite samples. Annealing in their experiments resulted in an increase of the mean grain-size by a factor of 2–5 by continuous grain growth. The CPO preserved its orientation but decreased in strength. However, other studies on quartz have found that *c*-axis orientations may be modified during annealing by orientation-dependent growth, resulting in increased CPO strength (Green, 1967), or modification of the *c*-axis CPO from a dominant point maxima to a broader girdled circle in the direction of applied compression (Gleason and Tullis, 1990; Green II et al., 1970). Stöckhert and Duyster (1999) have documented a transient stage of discontinuous grain growth in quartz veins. The porphyroblasts in their study have a distinctly different CPO than the surrounding matrix grains. The authors postulate that the discontinuous grain growth was promoted by the pre-existing CPO of the matrix and the variation of the grain-boundary energy with misorientation angle (Stöckhert and Duyster, 1999). Similar interpretations were made recently for chromite (Ghosh et al., 2017) and ice (Hidas et al., 2017). In ice, GBM was interpreted to weaken and even reset the CPO during grain-growth (Samyn et al., 2008; Wilson, 1982), and to produce a girdle of *c*-axis orientations with an angle to the compression axis during syn-deformational GBM (Montagnat et al., 2015). Additional grain growth experiments on calcite and rock-analogue materials such as octachloropropane have generally concluded that the post-annealing CPO may be weaker but is overall similar to the original CPO (Park et al., 2001; Wilson, 1982). In summary, some studies conclude that during annealing the initial CPO is preserved, while others, show that the CPO can be modified in terms of its strength and/or its orientation.

4.3. Implications for CPO evolution and seismic anisotropy

It is well-documented that shear deformation of olivine typically leads to strengthening and rotation of CPO, which under a wide range of conditions will align the olivine [100] axes with the direction of flow (Kaminski and Ribe, 2001; Skemer et al., 2012; Wenk et al., 1991; Zhang and Karato, 1995). The process of aligning olivine grains is complex, however, as it reflects the competition between several deformation and recovery processes. Through deformation, the 'primary' CPO is aligned with the deformation kinematics while recovery processes, like dynamic recrystallization, are overcome by crystallographic rotation due to plastic deformation (Karato, 1987). Zhang et al. (2000) demonstrated that during deformation and associated dynamic recrystallization, a fraction of olivine grains with low dislocation-density and low Schmid factor (i.e., the resolved shear stress on the [100](010) slip system) tend to grow at the expense of adjacent grains with high

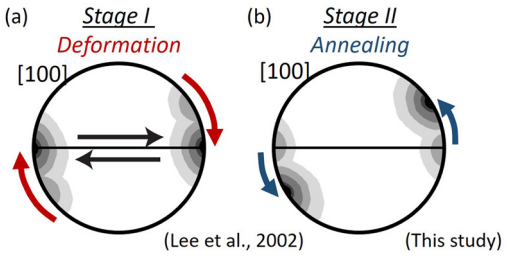

Fig. 4. Schematic illustration depicting the stages for olivine [100] CPO during (a) deformation and (b) subsequent annealing. (a) Stage I – During deformation, after sufficient strain, the dominant peak is aligned with the shear direction. A secondary peak on the plane of rotation is interpreted to result from syndeformational grain-boundary migration (Lee et al., 2002; Zhang et al., 2000). (b) Stage II – During annealing subsequent to stage I, a reversal occurs in which the secondary peak, at an angle to the shear direction, becomes dominant on the expense of the original peak.

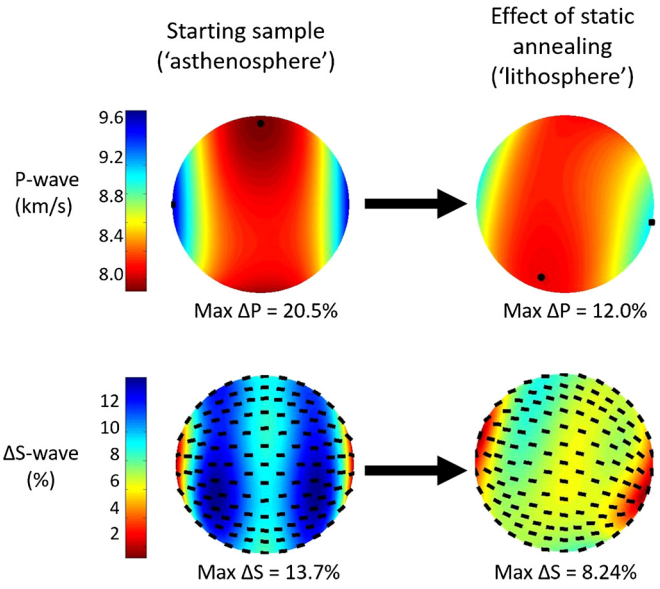

Fig. 5. Modification of the anisotropic signature of seismic waves due to static annealing of an olivine polycrystal with pre-existing CPO. Pole figures show the orientation distributions of P-wave velocities (top) and the magnitudes and polarization directions of S-waves (bottom). The deformed starting sample, PT0178, is analogous to deformed asthenosphere with a strong A-type CPO. The CPO of porphyrobstast grains (i.e., Fig. 2c) is analogous to a lithospheric layer after cooling and the cessation of deformation at asthenospheric temperatures. Pole figures were calculated using MSAT (Walker and Wookey, 2012) using elastic constants for olivine from Abramson et al. (1997).

dislocation-density and high Schmid factor. This fraction of grains with low dislocation density form a secondary peak in the [100] pole figure (Fig. 4a), which is also seen in many natural samples (e.g., Ben Ismaïl and Mainprice, 1998), and is interpreted to result from syn-deformational GBM (Kaminski and Ribe, 2001; Lee et al., 2002). Experimental studies to shear strains of $\gamma \sim 1.5$ demonstrate that this secondary peak weakens with progressive deformation and the primary point maximum emerges parallel to the shear direction (Zhang and Karato, 1995).

In our annealing experiments, we observe that a reversal of the CPO evolution arises due to extensive recovery by GBM for initially highly-strained aggregates. Starting from the orientation of a typical olivine A-type fabric, we observe growth of grains that are misoriented with respect to the original CPO (Fig. 4b). This produces a secondary peak in the [100] pole figure that strengthens with annealing time (Figs. 1 and 4). At some point between 20 and 168 h, this secondary, oblique peak becomes dominant (Figs. 1 and 4), modifying the associated seismological signature (Fig. 5).

While CPO in the asthenosphere potentially records the composite signature of both previous and current deformation events (Boneh et al., 2015), CPO in the lithosphere is often interpreted to record past deformation events and remain unmodified by ongoing deformation in the underlying asthenosphere (Deschamps et al., 2008). This 'frozen' or 'fossil' texture, can significantly affect the overall seismic signature of the upper mantle. However, it is unclear whether, for example, seismic anisotropy generated in the lithosphere truly reflects CPO introduced near mid-ocean ridges, or if additional modification has occurred. In this study, we have demonstrated that CPO may continue to evolve under static conditions due to preferential growth of grains in particular orientations. Fig. 5 reveals the consequences of microstructural evolution during annealing on P-wave velocities and anisotropy of S-wave velocities. In a dunite with the CPO of the deformed sample PT0718, P-wave anisotropy is approximately 20%. In contrast, in dunite with the CPO of the porphyroblast grains (Fig. 2c), P-waves would exhibit anisotropy of only 12%. S-wave anisotropy is similarly reduced, from 13.7% to 8.2%. Moreover, the orientations of the fast direction are rotated by 10–15 degrees. These changes in the orientation distributions and magnitudes of seismic anisotropy offer an explanation for the general global trend of greater seismic anisotropy in the asthenosphere compared with the lithosphere (Beghein et al., 2014; Burgos et al., 2014).

5. Conclusions

CPO forms during creep by dislocation-mediated deformation mechanisms, and relationships between seismic anisotropy, CPO, and kinematics, are often used to infer flow patterns in the upper mantle (e.g., Karato et al., 2008; Skemer and Hansen, 2016). However, recent studies have shown that CPO doesn't necessarily record only the ongoing deformation but may retain a record of, or be otherwise influenced by, former deformation episodes (Blackman et al., 2002; Boneh et al., 2015; Boneh and Skemer, 2014; Hansen et al., 2014). Discontinuous grain-growth, which occurs readily during high-temperature annealing of textured olivine samples leads to significant modification of the CPO. This implies that CPO, and hence seismic anisotropy, will continue to evolve, even during periods of tectonic quiescence. These observations challenge the view that CPO in the lithosphere is frozen and generally remains unchanged. Interpretation of seismic anisotropy generated in the lithosphere must consider that CPO formed under asthenospheric temperatures and incorporated into the lithosphere may have weakened and rotated with time.

Acknowledgements

The authors thanks Gayle Gleason for enriching discussions and to Manuele Faccenda and anonymous reviewer for their constructive comments. This research is supported by NSF EAR-1131985 (to PS), with additional support from the Institute of Materials Science and Engineering at Washington University in St. Louis. DW and LNH acknowledge support from the Natural Environment Research Council Grant NE/M000966/1.

Appendix A

Mobility is a fundamental property of grain boundaries and may be used to model grain-growth and other processes. To estimate the mobility of the large olivine grain boundary in Fig. 3 we use the following relation for the velocity of a moving interface (V)

$$V = MF \tag{1}$$

where M is the grain boundary mobility, which has an Arrhenius form ($M = M_0 e^{-E/RT}$), and F is the driving force per unit area. We assume the driving force for grain boundary migration results from both the difference in grain boundary energy and the difference in strain energy between the abnormally growing grain and the matrix. The driving force per unit area due to grain boundary energy is expressed as:

$$F_b = 3\gamma/d, \tag{2}$$

where γ is the grain-boundary energy (~0.9 J/m^2 for olivine; Cooper and Kohlstedt, 1984), and d is the diameter of the matrix grains. The driving force per unit area due to strain energy is given by:

$$F_s = \mu b^2 (\Delta\rho), \tag{3}$$

where μ is the shear modulus, b is the length of the Burgers vector, and $\Delta\rho$ is the difference in dislocation-density across the boundary of interest. We sum the driving forces due to the grain-boundary and strain energies ($F = F_b + F_s$). Using equations (2) and (3), and $\mu = 50$ GPa and $b = 0.6$ nm, we calculate the grain boundary surface energy to be $2.5 \times 10^5 [\frac{N}{m^2}]$, the strain energy to be $1.0 \times 10^7 [\frac{N}{m^2}]$. The grain boundary velocity is assumed to be constant through the duration of the experiment:

$$V = \frac{d_p - d}{dt} \tag{4}$$

where d_p is the final diameter of the porphyroblast highlighted in Fig. 3, d is the mean diameter of the matrix grains, and dt is the duration of the experiment during which temperature was at its maximum. V is calculated to be 6.9×10^{-9} m/s. From equation (1) grain-boundary mobility is calculated to be $M_b = 6.6 \times 10^{-16}$ $[\frac{m^3}{Ns}]$ at the experimental temperature of 1250 °C. This value can be compared with grain boundary mobility for Fo_{92} olivine determined by Cooper and Kohlstedt (1984), who calculate $M_b = 1.6 \times 10^{-15}$ $[\frac{m^3}{Ns}]$ and $M_b = 2.3 \times 10^{-15}$ $[\frac{m^3}{Ns}]$, at $T = 1300$ and 1400 °C respectively.

Appendix B. Supplementary material

Supplementary material related to this article can be found online at http://dx.doi.org/10.1016/j.epsl.2017.06.050.

References

Abbruzzese, G., Lücke, K., 1986. A theory of texture controlled grain growth, I: derivation and general discussion of the model. Acta Metall. 34, 905–914.
Abramson, E.H., Brown, M., Slutsky, L.J., Zaug, J., 1997. The elastic constants of San Carlos olivine up to 17 GPa. J. Geophys. Res. 102, 12,252–212,263.
Atkinson, H., 1988. Overview No. 65: theories of normal grain growth in pure single phase systems. Acta Metall. 36, 469–491.
Barruol, G., Helffrich, G., Vauchez, A., 1997. Shear wave splitting around the northern Atlantic: frozen Pangaean lithospheric anisotropy? Tectonophysics 279, 135–148.
Becker, T.W., Conrad, C.P., Schaeffer, A.J., Lebedev, S., 2014. Origin of azimuthal seismic anisotropy in oceanic plates and mantle. Earth Planet. Sci. Lett. 401, 236–250.
Beghein, C., Yuan, K., Schmerr, N., Xing, Z., 2014. Changes in seismic anisotropy shed light on the nature of the Gutenberg discontinuity. Science 343, 1237–1240.
Ben Ismaïl, W., Mainprice, D., 1998. An olivine fabric database: an overview of upper mantle fabrics and seismic anisotropy. Tectonophysics 296, 145–157.
Bhattacharyya, J., Agnew, S., Muralidharan, G., 2015. Texture enhancement during grain growth of magnesium alloy AZ31B. Acta Mater. 86, 80–94.
Blackman, D.K., Wenk, H., Kendall, J.M., 2002. Seismic anisotropy of the upper mantle, 1: factors that affect mineral texture and effective elastic properties. Geochem. Geophys. Geosyst. 3, 1–24.
Boneh, Y., Morales, L.F., Kaminski, E., Skemer, P., 2015. Modeling olivine CPO evolution with complex deformation histories: implications for the interpretation of seismic anisotropy in the mantle. Geochem. Geophys. Geosyst. 16, 3436–3455.
Boneh, Y., Skemer, P., 2014. The effect of deformation history on the evolution of olivine CPO. Earth Planet. Sci. Lett. 406, 213–222.
Burgos, G., Montagner, J.P., Beucler, E., Capdeville, Y., Mocquet, A., Drilleau, M., 2014. Oceanic lithosphere–asthenosphere boundary from surface wave dispersion data. J. Geophys. Res., Solid Earth 119, 1079–1093.

Cooper, R., Kohlstedt, D., 1984. Sintering of olivine and olivine–basalt aggregates. Phys. Chem. Miner. 11, 5–16.
Deschamps, F., Lebedev, S., Meier, T., Trampert, J., 2008. Stratified seismic anisotropy reveals past and present deformation beneath the East-central United States. Earth Planet. Sci. Lett. 274, 489–498.
Eichelkraut, H., Abbruzzese, G., Lücke, K., 1988. A theory of texture controlled grain growth, II: numerical and analytical treatment of grain growth in the presence of two texture components. Acta Metall. 36, 55–68.
Evans, B., Renner, J., Hirth, G., 2001. A few remarks on the kinetics of static grain growth in rocks. Int. J. Earth Sci. 90, 88–103.
Ghosh, B., Misra, S., Morishita, T., 2017. Plastic deformation and post-deformation annealing in chromite: mechanisms and implications. Am. Mineral. 102, 216–226.
Gleason, G., Tullis, J., 1990. The effect of annealing on the lattice preferred orientations of deformed quartz aggregates. EOS, Trans. Am. Geophys. Union 71, 1657.
Green, H., 1967. Quartz: extreme preferred orientation produced by annealing. Science 157, 1444–1447.
Green II, H., Griggs, D., Christie, J., 1970. Syntectonic and annealing recrystallization of fine-grained quartz aggregates. In: Experimental and Natural Rock Deformation/Experimentelle und natürliche Gesteinsverformung. Springer, pp. 272–335.
Hansen, L.N., Warren, J.M., Zimmerman, M.E., Kohlstedt, D.L., 2016. Viscous anisotropy of textured olivine aggregates, part 1: measurement of the magnitude and evolution of anisotropy. Earth Planet. Sci. Lett. 445, 92–103.
Hansen, L.N., Zhao, Y.-H., Zimmerman, M.E., Kohlstedt, D.L., 2014. Protracted fabric evolution in olivine: implications for the relationship among strain, crystallographic fabric, and seismic anisotropy. Earth Planet. Sci. Lett. 387, 157–168.
Heilbronner, R., Tullis, J., 2002. The effect of static annealing on microstructures and crystallographic preferred orientations of quartzites experimentally deformed in axial compression and shear. Geol. Soc. (Lond.) Spec. Publ. 200, 191–218.
Hidas, K., Tommasi, A., Mainprice, D., Chauve, T., Barou, F., Montagnat, M., 2017. Microstructural evolution during thermal annealing of ice-I h. J. Struct. Geol. 99, 31–44.
Hillert, M., 1965. On the theory of normal and abnormal grain growth. Acta Metall. 13, 227–238.
Humphreys, F., 1997. A unified theory of recovery, recrystallization and grain growth, based on the stability and growth of cellular microstructures, I: the basic model. Acta Mater. 45, 4231–4240.
Jung, H., Karato, S.-i., 2001. Water-induced fabric transitions in olivine. Science 293, 1460–1463.
Kaminski, É., Ribe, N.M., 2001. A kinematic model for recrystallization and texture development in olivine polycrystals. Earth Planet. Sci. Lett. 189, 253–267.
Karato, S., 1989. Grain growth kinetics in olivine aggregates. Tectonophysics 168, 255–273.
Karato, S.-i., Jung, H., Katayama, I., Skemer, P., 2008. Geodynamic significance of seismic anisotropy of the upper mantle: new insights from laboratory studies. Annu. Rev. Earth Planet. Sci. 36, 59–95.
Karato, S.I., 1987. Seismic anisotropy due to lattice preferred orientation of minerals: kinematic or dynamic? In: High-Pressure Research in Mineral Physics: A Volume in Honor of Syun-iti Akimoto, pp. 455–471.
Kim, H.-C., Kang, C.-G., Huh, M.-Y., Engler, O., 2007. Effect of primary recrystallization texture on abnormal grain growth in an aluminum alloy. Scr. Mater. 57, 325–327.
Lee, K.-H., Jian, Z., Karato, S.-i., 2002. A scanning electron microscope study of the effects of dynamic recrystallisation on lattice preferred orientation in olivine. Tectonophysics 351, 331–341.
Lin, P.-Y.P., Gaherty, J.B., Jin, G., Collins, J.A., Lizarralde, D., Evans, R.L., Hirth, G., 2016. High-resolution seismic constraints on flow dynamics in the oceanic asthenosphere. Nature.
Mainprice, D., Bachmann, F., Hielscher, R., Schaeben, H., 2014. Descriptive tools for the analysis of texture projects with large datasets using MTEX: strength, symmetry and components. Geol. Soc. (Lond.) Spec. Publ. 409 (SP409), 408.
Mishin, O., Jensen, D.J., Hansen, N., 2010. Evolution of microstructure and texture during annealing of aluminum AA1050 cold rolled to high and ultrahigh strains. Metall. Mater. Trans. A, Phys. Metall. Mater. Sci. 41, 2936–2948.
Montagnat, M., Chauve, T., Barou, F., Tommasi, A., Beausir, B., Fressengeas, C., 2015. Analysis of dynamic recrystallization of ice from EBSD orientation mapping. Front. Earth Sci. 3, 81.
Nichols, S.J., Mackwell, S.J., 1991. Grain growth in porous olivine aggregates. Phys. Chem. Miner. 18, 269–278.
Nicolas, A., Christensen, N.I., 1987. Formation of anisotropy in upper mantle peridotites – a review. In: Fuchs, K., Froidevaux, C. (Eds.), Composition, Structure and Dynamics of the Lithosphere–Astenosphere System. AGU, Washington, DC.
Novikov, V., Novikov, V.I.U.r.e., 1997. Grain Growth and Control of Microstructure and Texture in Polycrystalline Materials. CRC.
Park, Y., Ree, J.-H., Kim, S., 2001. Lattice preferred orientation in deformed-then-annealed material: observations from experimental and natural polycrystalline aggregates. Int. J. Earth Sci. 90, 127–135.
Powers, J., Glaeser, A., 1998. Grain boundary migration in ceramics. Interface Sci. 6, 23–39.
Rios, P.R., 1997. Abnormal grain growth development from uniform grain size distributions. Acta Mater. 45, 1785–1789.
Rollett, A., Srolovitz, D., Anderson, M., 1989. Simulation and theory of abnormal grain growth – anisotropic grain boundary energies and mobilities. Acta Metall. 37, 1227–1240.
Samyn, D., Svensson, A., Fitzsimons, S., 2008. Dynamic implications of discontinuous recrystallization in cold basal ice: Taylor Glacier, Antarctica. J. Geophys. Res., Earth Surf. 113.
Silver, P.G., Chan, W.W., 1991. Shear wave splitting and subcontinental mantle deformation. J. Geophys. Res., Solid Earth 96, 16429–16454.
Silver, P.G., Savage, M.K., 1994. The interpretation of shear-wave splitting parameters in the presence of two anisotropic layers. Geophys. J. Int. 119, 949–963.
Skemer, P., Hansen, L.N., 2016. Inferring upper-mantle flow from seismic anisotropy: an experimental perspective. Tectonophysics 668, 1–14.
Skemer, P., Karato, S.-i., 2007. Effects of solute segregation on the grain-growth kinetics of orthopyroxene with implications for the deformation of the upper mantle. Phys. Earth Planet. Inter. 164, 186–196.
Skemer, P., Warren, J.M., Hirth, G., 2012. The influence of deformation history on the interpretation of seismic anisotropy. Geochem. Geophys. Geosyst. 13.
Stöckhert, B., Duyster, J., 1999. Discontinuous grain growth in recrystallised vein quartz – implications for grain boundary structure, grain boundary mobility, crystallographic preferred orientation, and stress history. J. Struct. Geol. 21, 1477–1490.
Walker, A.M., Wookey, J., 2012. MSAT – a new toolkit for the analysis of elastic and seismic anisotropy. Comput. Geosci. 49, 81–90.
Wallis, D., Hansen, L.N., Ben Britton, T., Wilkinson, A.J., 2016. Geometrically necessary dislocation densities in olivine obtained using high-angular resolution electron backscatter diffraction. Ultramicroscopy 168, 34–45.
Wenk, H.R., Bennett, K., Canova, G.R., Molinari, A., 1991. Modelling plastic deformation of peridotite with the self-consistent theory. J. Geophys. Res. 96, 8337–8349.
Wilkinson, A.J., Meaden, G., Dingley, D.J., 2006. High resolution mapping of strains and rotations using electron backscatter diffraction. Mater. Sci. Technol. 22, 1271–1278.
Wilson, C., 1982. Texture and grain growth during the annealing of ice. Textures Microstruct. 5, 19–31.
Yuan, H., Romanowicz, B., 2010. Lithospheric layering in the North American craton. Nature 466, 1063–1068.
Zahid, G., Huang, Y., Prangnell, P., 2009. Microstructure and texture evolution during annealing a cryogenic-SPD processed Al-alloy with a nanoscale lamellar HAGB grain structure. Acta Mater. 57, 3509–3521.
Zhang, S., Karato, S.-i., 1995. Lattice preferred orientation of olivine aggregates deformed in simple shear. Nature 375, 774–777.
Zhang, S., Karato, S.-i., Fitzgerald, J., Faul, U.H., Zhou, Y., 2000. Simple shear deformation of olivine aggregates. Tectonophysics 316, 133–152.
Zhao, Y.-H., Zimmerman, M.E., Kohlstedt, D.L., 2009. Effect of iron content on the creep behavior of olivine, 1: anhydrous conditions. Earth Planet. Sci. Lett. 287, 229–240.